SPE 71610

Use of Satellite Radar Images in Surveillance and Control of Two Giant Oilfields in California

Tad W. Patzek[1], SPE Member, Dmitriy B. Silin[2], and Eric Fielding[3]

[1]University of California at Berkeley and Lawrence Berkeley National Laboratory; patzek@patzek.berkeley.edu, http://patzek.berkeley.edu
[2]Lawrence Berkeley National Laboratory, dsilin@lbl.gov
[3]Jet Propulsion Laboratory, California Institute of Technology, ericf@sierras.jpl.nasa.gov

This paper was prepared for presentation at the SPE Annual Technical Conference and Exhibition held in New Orleans, 30 September – 3 October 2001.

This paper was selected for presentation by an SPE Program Committee following review of information contained in an abstract submitted by the author(s). Contents of the paper, as presented, have not been reviewed by the Society of Petroleum Engineers and are subject to correction by the author(s). The material, as presented, does not necessarily reflect any position of the Society of Petroleum Engineers, its officers, or members. Papers presented at SPE meetings are subject to publication review by Editorial Committees of the Society of Petroleum Engineers. Electronic reproduction, distribution, or storage of any part of this paper for commercial purposes without the written consent of the Society of Petroleum Engineers is prohibited. Permission to reproduce in print is restricted to an abstract of not more than 300 words; illustrations may not be copied. The abstract must contain conspicuous acknowledgment of where and by whom the paper was presented. Write Librarian, SPE, P.O. Box 833836, Richardson, TX 75083-3836, U.S.A., fax 01-972-952-9435.

Abstract.

A global analysis of the evolution of an entire giant oilfield is now feasible. The oilfield can be viewed as a single complex system consisting of reservoir rock and fluids, and coupled injectors and producers. The vertically averaged areal signatures of primary and waterflood projects in the field can be tracked in time as the displacement of ground surface above these projects. The Synthetic Aperture Radar interferograms (InSAR) from satellites are the enabling technology. In this paper, we add a new element to our multilevel, integrated surveillance and control system: time-lapse satellite InSAR images of the oilfield surface. In particular, we analyze ten differential InSAR images of the South/North Belridge and Lost Hills diatomite fields, CA, between 04/95 and 12/99. The images have been reprocessed and normalized to obtain the ground surface displacement rate. In return, we have been able to calculate section-by-section the net subsidence of ground surface over the entire field areas. The calculated subsidence volumes are thought to be close to the subsidence at the tops of the reservoirs. The images show that the rate of subsidence has decreased in some parts of Lost Hills and Belridge, while it increased in others. Using the production and injection data from the California Conservation Commission and Chevron, we have been able to demonstrate the remarkable behavior of both fields: (1) There is recirculation of injected water through the "tubes" of damaged soft rock that link injectors with producers, resulting in diminished pressure support from the waterfloods. (2) Consequently, despite more water injection, there is more subsidence in Sections 29, 34, and 33 in Belridge and in Sections 29, 4, 5, and 32 in Lost Hills. (3) As much of the injected water is recirculated, the rate of subsidence is proportional to water production rate. (4) Compaction remains an important mechanism of hydrocarbon production. (5) In addition to accelerated compaction in the densest and most advanced waterfloods, there is a sizable oil production response to water injection. Means of controlling and improving the existing waterfloods are discussed.

1. Introduction

A successful waterflood depends on the proper operation of individual wells in a pattern, on maintaining the balance between injection and production over the entire project or field, and on preventing well failures. It is very difficult to conduct a waterflood in a soft low-permeability rock such as chalk or diatomite, where rock damage and ensuing injector-producer linkage[1,2], uncontrolled growth of hydrofractures[3,4], and water breakthrough in thief layers are encountered[5,6].

Our paper deals with several large waterfloods in two low permeability, high porosity diatomaceous oilfields in California: South Belridge and Lost Hills. These two fields are shallow, have thousands of wells spaced every 50-350 ft, and have been researched more than perhaps any other oilfield in the world. All wells are hydrofractured, and the vertical "fractures[a]" are thought[9] to have tip-to-tip lengths of the order of 100-300 ft and heights of 50-300 ft, **Fig. 1**. Waterflood patterns are usually configured as staggered line drives, but these patterns not always follow the direction of maximum horizontal *in-situ* stress. Depending on the fracture orientation and flow direction, areal sweep by water may vary greatly[10]. Multiscale layering in the diatomite[11] and rock damage[12,13]

[a] In reality, the "hydrofractures" are volumes of pulverized soft rock with complex connectivity and geometry[3, 4, 7, 8].

result in strong anisotropy and nonuniform vertical and areal sweep.

If injected water does not provide uniform pressure support of the reservoir, differential rock compaction causes well failures. If the injected water does not sweep uniformly the reservoir volume, recovery efficiency of the waterflood decreases. High rate of well failure[12-14], **Fig. 2**, and low recovery efficiency combine to lower waterflood profitability.

Damage of heterogeneous soft rocks caused by water injection is not yet well understood nor quantified, but, as demonstrated here and elsewhere[15], it leads to an increased rate of rock compaction during water injection and poorer volumetric sweep by water. We assert that a soft rock reservoir cannot be waterflooded efficiently without the understanding and managing rock damage. Existing models of rock damage[8,16] need improvement and calibration.

As in preventive health care, it is important to diagnose the symptoms of uncontrolled rock damage early and to apply the cure on time. Our solution is to design[6,17-19] a multilevel, integrated system of surveillance and control, which acquires and processes waterflood data, and helps field personnel make optimal decisions, **Fig. 3**. Our systems for shallow oilfields (<9000 ft in depth) in arid surroundings may use the satellite Synthetic Aperture Radar interferograms (InSAR) of the field surface. The main goal of this paper is to familiarize petroleum engineers with the benefits of InSAR technology.

In the last few years, InSAR has become a very attractive technique to obtain more information from SAR images[20,21]. Both the amplitude of the signal and its phase are used. Usually, two SAR images of the same region are acquired with slightly different sensor positions, and coherently combined together. SAR interferometry can be performed either using data collected by repeat-pass or single-pass sensors. The former implies the same antenna is used twice while the latter requires two distinct antennas to be flown aboard the aircraft or satellite.

This paper focuses on ERS repeat-pass InSAR images acquired in 1994-99 for the giant Belridge Diatomite and Lost Hills[22] Diatomite fields, California, U.S.A. ERS-1, a satellite carrying a space borne C-band SAR (5.6 cm wavelength), was launched in July 1991, while ERS-2 was launched in April 1995. Both satellites were built by ESA (the European Space Agency), are identical from the SAR point of view, and they acquire data over the Earth with incidence angles varying between 19 deg and 26 deg with effective ground pixel spacing of 20 m for the Single Look Complex (SLC) product.

In petroleum industry, a promising application of SAR interferometry is to generate time-lapse surface deformation maps owing to the fact that the change of height can be related with great precision to the phase difference between two SAR images. The rate of surface displacement can then be combined with the overall volumetric balance of fluid injection to identify the areas with most imbalance and/or highest gas saturation. If information about vertical sweep by water is also available from cross-well images [23], then volumetric sweep can be estimated. This technique will be useful especially for relatively shallow waterfloods and very shallow steamfloods.

2. Processing of the SAR data

For a thorough review of the principles of imaging radar, see Refs.[20 24 25] and references therein. Briefly, imaging radar is an active illumination system, **Fig. 4**, side-looking with respect to the vehicle's direction of travel. The brightness (amplitude, A) of a reflected radar echo that has been transmitted from an antenna mounted on an aircraft or spacecraft, backscattered from the surface of the Earth, and received a fraction of a second later by the same antenna, is measured and recorded to construct the image, Table 3- Table 4. Let us consider an image to be a set of values $A(x, y)$, where the x-coordinate is in the direction of platform motion and the y-coordinate is in the direction of illumination. The value of y (related to the radar range) and its resolution is based on the arrival time of the echo, and the timing precision and pulse bandwidth of the radar, while the value of x (related to the radar azimuth) and its resolution depends on the position of the platform and the beam width of the radar. Since the beam-width is inversely related to antenna size, small (physically realizable) antennas tend to generate large footprints and their corresponding images have poor azimuthal resolution. Synthetic aperture radar (SAR) takes advantage of the Doppler history of the radar echoes generated by the forward motion of the vehicle to synthesize a large antenna, enabling high azimuthal resolution in the resulting image despite a physically small antenna.

Even though a typical radar image displays only amplitude data, the aspect of SAR most important here is its *coherence*, i.e., retention of both amplitude and phase information in the radar echo during data acquisition and subsequent processing. The details of SAR interferometry are summarized in **Appendix A**. There, we examine estimation of topographic height from the differential range measured by two radar antennas looking at the same surface, followed by a discussion of *changes* in topography (surface displacement) based on range change in two or more successive SAR images.

Interferometric processing of complex SAR data combines two single look complex (with amplitude and phase) images into an interferogram. First, the two images are co-registered (aligned), and their amplitudes and phases are adjusted by interpolation. In the same step common band-filtering of the azimuth and range spectra can be conducted, in order to include only those parts of the spectra which are common to the two images, and thereby optimize the interferometric correlation and minimize the effects of the baseline geometry on the interferometric correlation. Then the two images are cross-correlated, i.e., the normalized complex interferogram is computed. The interferogram displays the phase difference information. The azimuth and range phase trends expected for a flat or spherical Earth are removed from the interferogram. From this “flattened” interferogram and the two registered intensity images the multi-look interferometric correlation and

backscatter intensities are estimated. The interferogram phase is further "unwrapped" to solve for the integer number of wavelengths wrapped into it, and to obtain the absolute range.

The InSAR phase difference is proportional to the change in range or distance between the antenna and the ground surface. A single interferogram thus measures only one component of the 3D motion of the surface. For ground subsidence, the ground surface displacement is primarily vertical, so we can estimate the vertical displacement from the InSAR range change by dividing by the cosine of the SAR incidence angle (angle with the vertical).

3. Application of InSAR to the Belridge and Lost Hills diatomite waterfloods

This paper is an initial attempt to bring together the satellite images of the field surface and the volumetric balance of injection and withdrawal. Obviously, more work needs to be done and our conclusions will be modified as our understanding of the correlation between surface displacement, reservoir rock damage, and waterflood performance improves.

3.1 Reservoir Description. The late and middle Miocene diatomaceous oil fields in the San Joaquin Valley, California, are located in Kern County, some forty miles west of Bakersfield. An estimated original-oil-in-place in the Monterey diatomaceous fields exceeds 10 billion barrels and is comparable to that in Prudhoe Bay in Alaska.

In Belridge, cyclic bedding of the diatomite is a well-documented phenomenon[11], attributed to alternating deposition of detritus beds, clay, and biogenic beds. The cycles span length-scales that range from a fraction of an inch to tens of feet, reflecting the duration of depositional phases from semi-annual to thousands of years. On a large scale, there are at least eight distinct oil producing layers (Cycles G-N) with good lateral continuity within each layer, but little vertical continuity between adjacent layers. The undamaged diatomite is very porous and nearly impermeable, Table 1. The high porosity and oil saturation, together with the large thickness and area translate into the gigantic oil-in-place estimates. Compared with South Belridge, the Lost Hills diatomite[26] contains more silt and clays.

To compensate for the low reservoir permeability, all wells in the diatomite are hydrofractured. A typical well has 2-8 fractures with a target fracture half-length of 50-150 feet. Wells are often spaced along lines following the maximum *in-situ* stress every 330 ft (2-1/2 acre) 165 feet (1-1/4 acre), 82 feet (5/8 acre), or even smaller. Thousands of hydrofractures have been already induced and thousands more may be created as waterflood and steam drive projects on 5/8 acre or smaller spacing are being introduced. The injector "hydrofractures" in the diatomite may link with the producers[1], and they grow[2-4,6,7,19].

With reasonable estimates of the *undamaged* diatomite layer properties at South Belridge (or in Lost Hills), Table 2, it may take 10-100 years to propagate pressure from an injector to a producer. Consequently, waterflood projects that rely on rock compressibility and water imbibition into the diatomite, and avoid early water breakthrough may take over 100 years to complete. Field evidence demonstrates, however, that tracers can flow from an injector to the surrounding producers in a matter of days[27]. Therefore, aggressive water injection, with water flow in "tubes" of damaged rock, fails to provide full pressure support over the entire diatomite column and alleviate subsidence.

Oil and water production rates as well as water injection rate in the Belridge diatomite are shown in **Fig. 5**. The most striking feature of this plot is balance of annual injection and production since 1989 and a robust water response to the increased injection in 1995. Similar trends in water production are seen in Lost Hills.

3.2 Surface Displacement. Because of the slow propagation of pressure from the injectors, increasing rock damage, and the simultaneous fluid withdrawal at the producers, subsidence has been a severe problem in Belridge[28]. As illustrated in Ref.[29], the maximum rate of subsidence in the last decade, measured by triangulation of obelisks, could be higher than that experienced earlier.

The InSAR images of Lost Hills and Belridge provide wealth of high-resolution information about surface displacement compared with the old monument data. The rate of surface displacement can now be calculated in monthly intervals over *each section* of the *entire* field. The resulting net subsidence can then be calculated over the entire field area with a higher precision than ever before. The areas outside of the active subsidence can be used for a zero level to a large extent. Unfortunately, because of the atmosphere the phase is not constant. In the images for the 98/11-98/8 interferograms, there are variations of up to about 0.4 mm/day equivalent outside of the two oil fields. We chose an approximate zero for the whole scene, but any detailed local analysis should probably use a local zero based on the area nearby. There are some spatial variations of the atmosphere over short distances similar to the oil field signal that we cannot remove and must consider to be a source of noise.

Fig. 5 - Fig. 8 show the rate of subsidence in mm/day in Lost Hills and Belridge in 1995, 1996 and 1998. We have assumed that the ground displacement is purely vertical to convert the SAR range change to subsidence for these figures. Between 1995 and 1999, the rate of subsidence in Lost Hills slowed down significantly. In Belridge, the rate of subsidence was about the same in 1995 and 1996, and it accelerated by 1999. The shaded spot in the August/November 1998 interferogram denote the area South Belridge Sections 34, 2, and 3, in which the subsidence rate was so high that the interferogram became decorrelated within the 105-day interval.

In 1999, a detailed analysis of subsidence by section, **Fig. 9**, shows that three sections in South Belridge (33, 2 and 29) had cumulative subsidence that exceeded the maximum subsidence in Lost Hills (Section 32). In general, the rates of

subsidence (slopes of each curve) in Lost Hills were lower than those in Belridge. In 1998/99 (over 380 days), the overall net surface subsidence in Belridge amounted to about 19.1 million barrels[29]. In the same time interval, the overall net surface subsidence in Lost Hills was about 5.1 million barrels. From the calculations by Hansen *et al*.[28], it follows that subsidence at the reservoir top in Belridge is close to that at the surface. As demonstrated through tiltmeter measurements by De Rouffignac and Bondor[13], the elastoplastic rock deformation that occurs immediately after injection or depletion appears to be the main cause of surface subsidence. The time-dependent creep deformation of the diatomaceous rock is responsible for the delayed subsidence. Therefore, we may assume that in Belridge and Lost Hills the net reservoir-level compaction was *at least* 18.3 and 4.9 million barrels, respectively, in 1999. To put these numbers in perspective, the subsided volume in Belridge was equal to about 40% of annual water injection in 1999. Fewer producers per acre caused less subsidence at Lost Hills. It is also possible that curtailment of steam injection in the Tulare sands overlying the South Belridge diatomite has resulted in additional surface subsidence. On the other hand, the Lost Hills diatomite is on average twice as deep as the South Belridge diatomite, and surface signature of the reservoir level subsidence is less there. In Fig. 9, the cumulative subsidence below 0.2 million bbl per year is subject to a large relative error, and should be disregarded.

3.3 Correlation of production and injection data with subsidence. Our well information, injection and production data for the Belridge diatomite are public domain and have been obtained from the California Conservancy Commission (CCCOGP). The corresponding Lost Hills data were obtained from Chevron for all sections and from CCCOGP for Section 4, where Aera Energy has a substantial waterflood operation. Thus, the cumulative production and well numbers in the Lost Hills diatomite sections reported here are for the Chevron operations only, with the exception of Section 4.

When surface displacement is averaged on the 20-by-20 meter pixels over the entire field area, roughly 10 pixels fall onto a single 1-1/4 acre pattern area. Therefore, it is tempting to relate surface subsidence to the local injection and withdrawal. In this paper, we analyze the 1999 injection and production in each section, and relate them to the 1999 subsidence. For injection control purpose, a similar analysis will be done for each Section 32 waterflood pattern in Lost Hills.

We start from comparing water production and injection by section, Fig. 10. In 1999, most Belridge sections produced about 80 percent of the injected water. There were two visible outliers: Section 2, which produced about 3 times more water than injected, and Section 19, in which twice as much water was injected as produced. Section 2 may be showing the symptoms of water encroachment from the adjacent waterfloods. Section 19 shows signs of above-average sweep efficiency by the injected water that kept replacing the initial gas saturation. In Lost Hills, each section produces about 70 percent of the injected water. In Section 32, 80 percent of the injected water was produced in 1999. Thus, Section 32 in Lost Hills behaves similarly to comparably advanced waterfloods in South Belridge.

Fig. 11 shows a startling picture of the inability of waterfloods to slow down subsidence in South Belridge and Lost Hills by the end of 1999. In a waterflood that provides pressure support, less subsidence should result from more water injection. This is the behavior of the Belridge section waterfloods that follow the horizontal trend, e.g., Sections 3 and 2. The denser and more advanced waterfloods in the South Belridge Sections 34, 29 and 33 bifurcate from this trend: there, more water injection causes more subsidence! In Lost Hills, Section 4 and 32 waterfloods follow a similar trend. Fig. 11 demonstrates that competition between more injection and more withdrawal in denser waterfloods is won by the withdrawal. Without rock damage, the low permeability diatomite simply does not imbibe enough water to provide full pressure support within a few years. With the rock damage, water is injected at a higher rate, but much of the water travels through the pulverized rock "tubes" to the producers without pressuring the rock matrix. One should remember, however, that the alternative to rock damage might be injection and production at economically infeasible rates.

In our opinion, Fig. 10 and Fig. 11 demonstrate that water injection causes damage to the diatomaceous rock. The damaged rock channels injected water to the producers, resulting in (1) high water production, and (2) less pressure support. At the same time, water imbibes from the multiple flow tubes into the rock matrix and displaces oil in countercurrent imbibition. Therefore, there must be an oil production response to waterflood. In the future, the key to waterflood success in the diatomite (or another low permeability, weak rock) will be to control water injection in such a way so as to create as many separate flow tubes as possible and maximize countercurrent imbibition. This cannot be achieved with a brute force water injection policy and simple pressure steps. Note that Section 19 in Belridge is an outlier: over 7 times more water was injected there compared with Section 3. Again, this behavior may be caused by resaturation of gas filled pores without early water breakthrough.

Fig. 12 amplifies the notion of rock damage playing a significant role in the diatomite. Again, more subsidence corresponds to more water produced in the water-flooded sections. Several sections in Lost Hills that are on primary follow a different water production trend. Sections 12 and 19 in Belridge are outliers and produced more water. Section 2 in Belridge, with only 30 injectors, produces less water than the trend.

Fig. 13 shows the total hydrocarbon production by section versus annual subsidence. In both fields, the general trend is that more hydrocarbon production causes more subsidence, but a plateau is reached ultimately, i.e., more subsidence does

not necessarily result in more hydrocarbon production. Section 33 in South Belridge is an outlier. It produced two times more hydrocarbons than Section 29 with only 20 percent more subsidence. Therefore, there is a stronger oil response in Section 33 than in Section 29, but there are also more wells and an older waterflood. Section 2 in Belridge is lagging the trend.

Fig. 11 - Fig. 13 hide the effect of the number of producing and injecting wells on the subsidence, and total water and hydrocarbon production. For example, in 1999, in South Belridge Section 2 there were 153 producers, and 20 injectors, while in Section 33 there were 458 producers and 164 injectors. Therefore, in Fig. 14 and Fig. 15, we plot the specific annual production per producing well in a given section versus the specific annual subsidence.

Fig. 14 plots the specific annual water and oil production versus the specific annual subsidence (per *producer*) in Belridge. Now Sections 29 and 33 that stood out in Fig. 12, are almost identical (their labels coincide) and produce less water with less subsidence per well than many other sections. In other words, infill slows down the rate of subsidence per injector. Sections 33, 34, 3 and 2 produce almost the same amount of hydrocarbons per well, but the specific subsidence is least in Section 33. Thus, waterflood in Section 33 provides more pressure support than in the other three sections that also show strong waterflood response. Sections 12 and 13 produce more water and less oil than any other section in Belridge. Thus, Fig. 14 may also reflect the general reservoir quality, which is best in the crestal sections 29 and 33, and clearly poorer in the Middle Belridge sections 12 and 13.

Fig. 15 plots the specific annual water and oil production vs. the specific annual subsidence in Lost Hills in 1999. Fig. 15 is similar to Fig. 14. Sections 33, 4 and 32 show comparable water production and increasing specific subsidence. Average producer in Section 32 produces more oil and subsides more than those in Sections 4 and 33. While the water and oil production per average well are comparable with South Belridge, the specific subsidence is somewhat less. We think that the lower specific subsidence in Lost Hills results from the lower producer density. The two factors distorting surface images of the reservoir top subsidence in both fields (cf. discussion of Fig. 9) cannot be ruled out. With time and well infills, the Lost Hills waterfloods will likely resemble their Belridge counterparts.

Fig. 16 shows the specific annual water injection versus specific subsidence (per *injector*) in Belridge and Lost Hills. In general, there is more water injection and less subsidence per injector in Lost Hills than in Belridge. With the exception of Section 28 and 30, the Belridge injectors follow in general an expected trend whereby more injection per well results in less specific subsidence. In Lost Hills, a similar trend is observed.

4. Conclusions

For the first time, a global analysis of evolution of an entire giant oilfield has been possible. A shallow oilfield can now be treated as a large complex rock system with the coupled injectors and producers. The Synthetic Aperture Radar interferograms (InSAR) from satellites have been the enabling technology. The SAR interferograms are now available commercially.

Our initial evaluation shows that the InSAR images are a unique source of detailed and precise information about surface displacement over two giant oil fields, the South Belridge Diatomite and the Lost Hills Diatomite, both in California, USA. Using time-lapse differential interferograms, we were able to calculate net subsidence of the ground surface for one square-mile sections of each field. The interferogram figures make it very clear that analysis of the oilfield behavior on a section basis is not very accurate. The subsidence patterns are clearly cutting across the section boundaries and sometimes parts of a section are doing different things. In the future, the analysis has to be performed not only section-by-section, but also according to cross-sectional patterns suggested by the satellite images.

By using detailed production and injection data in conjunction with the interferograms, we have shown that in low permeability soft diatomite the competition between water injection for pressure support and withdrawal for oil recovery is ultimately won by the withdrawal. Two mechanisms cause this outcome. The first mechanism is the inability of the undamaged diatomite to imbibe water at a sufficiently high rate to provide both pressure support and a meaningful production response. Prolonged high-rate water injection causes inevitable damage of the diatomite and creates “tubes” of pulverized rock that link the injectors and producers. Much of the injected water flows in these tubes, while also imbibing into the rock. The ensuing countercurrent imbibition displaces oil into the tubes and results in increased oil production, but without full pressure support.

We propose to devise a global system of waterflood control that will help to create multiple and uniformly spaced flow tubes between the injectors and producers. Currently such a system does not exist, but with better understanding of soft rock damage and complex geometry of oil displacement by water, we should be able to implement it. We urge a crash effort to gain sufficient knowledge of damage propagation dynamics to design and implement the new control system. Otherwise, the exponentially increasing wellbore damage will curtail waterflood profitability and limit our options.

5. Acknowledgements

This work was sponsored by the DOE ORT Partnership under Contract DE-ACO3-76FS0098 to the Lawrence Berkeley National Laboratory. Partial support was also provided by gifts from Chevron to UC Oil, Berkeley. Portions of this work were performed at the Jet Propulsion Laboratory, California Institute of Technology under contract with the National Aeronautics and Space Administration. Extensive help with the Lost Hills diatomite data and many useful discussions with Mr. James Brink of Chevron USA are gratefully

acknowledged. We would also like to thank Dr. Phiroze Patel, Mr. David Mayer and Mr. Thomas Moroney of Aera Energy, LLC for their useful inputs into our work.

6. References

1. Patzek, T.W. *Paper SPE 24040, Surveillance of South Belridge Diatomite*. In *Proceedings of the Western Regional SPE Meeting*. 1992. Bakersfield, CA.
2. Patzek, T.W., and Silin, D. B., *Control of Water Injection into a Low-Permeability Rock. 1. Hydrofracture Growth.* Transport in Porous Media, 2001(TIPM-1492).
3. Kovscek, A.R., Johnston, M., and Patzek, T. W., *Interpretation of Hydrofracture Geometry Using Temperature Transients I: Model Formulation and Verification.* In Situ, 1996. **20**(3): p. 221-250.
4. Kovscek, A.R., Johnston, M., and Patzek, T. W., *Interpretation of Hydrofracture Geometry Using Temperature Transients II: Asymmetric Hydrofractures.* In Situ, 1996. **20**(3): p. 251-289.
5. Silin, D.B., and Patzek, T. W. *SPE 59300: Control of Water Injection into a Layered Formation*. In *2000 SPE/DOE Improved Oil Recovery Symposium*. 2000. Tulsa, OK.
6. Silin, D.B., and Patzek, T. W., *Control of Water Injection into a Layered Formation.* SPEJ, 2001(June).
7. Ilderton, D., Patzek, T. W., Rector, J. W., and Vinegar, H. J., *Microseismic Imaging of Hydrofractures in the Diatomite.* SPE Formation Evaluation J., 1996(March): p. 46-54.
8. Barenblatt, G.I., Prostokishin, V. M., *A mathematical model of damage accumulation taking into account microstructural effects.* Euro. Jnl of Mathematics, 1993. **4**: p. 225-240.
9. Wright, C.A., Davis, E. J., Golich, G. M., Ward, J. F., Demetrius, S. L., Minner, W. A., and Weijers, L. *SPE 46194, Downhole tiltmeter fracture mapping: finally measuring hydraulic fracture dimensions*. In *1998 SPE Western Regional Conference*. 1998. Bakersfield, CA.
10. Crawford, P.B., *Estimated effect of vertical hydrofractures on secondary recovery.* Petr. Trans. AIME, 1954. **201**: p. 192-196.
11. Schwartz, D.E., *Characterizing the Lithology, Petrophysical Properties, and Depositional Settings, South Belridge Field, Kern County, CA.*, in *Studies of the Geology of the San Joaquin Basin*, S.A. Graham, and Olson, H. C., Editor. 1988, The Pacific Section Society of Economic Paleontologists and Mineralogists: Los Angeles, CA.
12. De Rouffignac, E., and Bondor, P.L. *Land subsidence and well failure in the Belridge Diatomite oil field, Kern County, California. Part I. Experiments, model and verification*. In *Land Subsidence (Proceedings of the Fifth International Symposium on Land Subsidence)*. 1995. The Hague: IAHS.
13. Bondor, P.L., and De Rouffignac, E.,. *Land subsidence and well failure in the Belridge Diatomite oil field, Kern County, California. Part II. Applications*. In *Land Subsidence (Proceedings of the Fifth International Symposium on Land Subsidence)*. 1995. The Hague: IAHS.
14. Myer, L., et al., *Use of visualization techniques in analysis of well failures in diatomite reservoirs.* The Leading Edge, 1996. **15**(3): p. 185-190.
15. Cook, C.C., Anderson, M. A., Halle, G., Gislefoss, E., and Brown, G. R., *An approach to simulating the effects of water-induced compaction in a North Sea Reservoir.* SPE Reservoir Evaluation & Engineering, 2001. **4**(2): p. 121-128.
16. Kachanov, L.M., *Introduction to continuum damage mechanics*. 1986, Dordrecht: Martinus Nijhoff Publishers.
17. De, A., Silin, D. B., and Patzek, T. W. *SPE 59295: Waterflood surveillance and supervisory control*. In *2000 SPE/DOE Improved Oil Recovery Symposium*. 2000. Tulsa, OK.
18. Patzek, T.W., and De, A., *Lossy Transmission Line Model of Hydrofractured Well Dynamics.* J. Petr. Sci. and Eng., 2000. **25**(1-2): p. 59-77.
19. Silin, D.B., and Patzek, T.W., *Control of Water Injection into a Low-Permeability Rock - 2. Optimal Control.* Transport in Porous Media, 2001(TIPM-1493).
20. Bürgmann, R., Rosen, P. A., Fielding E. J., *Synthetic Aperture Radar Inerferometry to Measure Earth's Surface Topography and its Deformation.* Ann. Rev. Earth Planet. Sci., 2000. **28**: p. 169-209.
21. Borgeaud, M., and Wegmuller, U. *On the Use of ERS SAR Interferometry for the Retrieval of Geo- and Bio-Physical Information*. In *ERS SAR Interferometry Workshop 1996*. 1996. Remote Sensing Laboratories, University of Zürich.
22. Fielding, E.J., Blom, R.G., and Goldstein, R.M., *Rapid subsidence over oil fields measured by SAR interferometry.* Geophys. Res. Lett., 1998. **25**: p. 3215-3218.
23. Patzek, T.W., Wilt, M., and Hoversten, M.,. *Paper SPE 59529, Using Crosshole Electromagnetics (EM) for Reservoir Characterization and Waterflood Monitoring*. In *2000 SPE Permian Basin Oil and Gas Recovery Conference*. 1999. Midland, TX.
24. Jensen, H.L., Graham, L. J., Pocello, L. J., and Neith E. N., *Side-looking airborne radar.* Scientific American, 1977. **237**: p. 84-95.
25. Elachi, C., *Spaceborne imaging radar: geologic and oceanographic applications.* Science, 1980. **209**: p. 1073-1082.
26. Perri, P.R., Emanuele, M. A., Fong, W. S., and Morea, M. F. *SPE 62526: Lost Hills CO_2 pilot: Design, injectivity test results, and implementation*. In *2000 SPE/AAPG Western Regional Meeting*. 2000. Long Beach, CA.
27. Patzek, T.W., Zhou, D., and Brink J.L., *Evaluation of a tracer test in Lost Hills Section 32, Unpublished Report*, 2000, PV Technologies and Chevron Petroleum Technology Company: San Ramon, CA.
28. Hansen, .S., Prats, M., and Chan, C. K. *Finite-Element*

Modeling of Depletion-Induced Reservoir Compaction and Surface Subsidence in the South Belridge Oil Field, California. In *Western Regional Meeting of the SPE*. 1993. Anchorage, AL.

29. Patzek, T.W., and Silin, D. B. *Use of InSAR in Surveillance and Control of a Large Field Project*. In *21st Annual International Energy Agency Workshop and Symposium*. 2000. Edinburgh, Scotland: Hariott-Watts University.
30. Zwahlen, E.D., and Patzek, T. W., *Linear Transient Flow Solution for Primary Oil Recovery with Infill and Conversion to Water Injection.* In Situ, 1997. **21**(4): p. 297-331.
31. Goldstein, R.M., Zebker, H. A., and Werner, C., *Satellite radar interferometry: two-dimensional phase unwrapping.* Radio Science, 1988. **23**: p. 713-720.
32. Zebker, H., and Goldstein, R., *Topographic mapping from interferometric synthetic aperture radar observations.* J. Geophys. Research, 1986. **91**: p. 4993-5001.

Appendix A – Surface topography from SAR

Single-pass InSAR. Consider two radar antennas, A_1 and A_2, simultaneously scanning the Earth surface and separated by the baseline vector $\vec{B}$ of length B and angle α, with respect to horizontal, **Fig. 17**. In this example, the first antenna transmits and receives the radar signal, while the second one only receives. The phase difference between backscattered signals received by the two antennas is a function of viewing geometry and the elevation of point z above the reference surface $H = 0$. If the viewing geometry is known with sufficient accuracy, then the surface topography *z(y)* can be calculated from the phase measurement to a precision of several meters, assuming that we can solve ("unwrap") for the 2π ambiguity inherent in phase measurements. From geometry, it follows that

$$z(y) = H - R_1 \cos\theta \qquad (1)$$

where θ is the "look" angle of the radar with respect to vertical, and R_1 is the range.

From elementary trigonometry

$$R_2^2 = (R_1 + dR)^2 =$$
$$R_1^2 + B^2 - 2R_1 B(\sin\theta\cos\alpha\cos\psi - \sin\alpha\cos\theta) \qquad (2)$$
$$\sin(\alpha - \theta) \approx \frac{2R_1 dR + dR^2 - B^2}{2R_1 B}, \text{ when } \psi^2 << 2$$

where ψ is the angle between the *zy*-plane in Fig. 17 and plane A_1A_2C, measured along a horizontal plane through point A_1. For simplicity, we will assume here that this angle is small[b]. The two images are co-registered, i.e., aligned and rescaled, and the first one is multiplied by the complex conjugate of the second one. The result is an interferogram with the representation[c] $A_1A_2e^{i(\varphi_1-\varphi_2)} \approx A^2e^{i\varphi}$.

The fractional phase difference φ between the two antennas scales as

$$\frac{dR}{\lambda} = \frac{\varphi}{2\pi}, \qquad (3)$$

where λ is the signal wavelength. Note that the fractional phase $\varphi \in [0, 2\pi]$ leads to ambiguity in range. Additional techniques, such as "phase unwrapping," **Fig. 18**, are used to solve for the integer number of wavelengths to obtain absolute range [31].

Equations (1) - (3) can now be combined to express the unknown topography *z(y)* in terms of the observed phase difference and the radar system parameters:

$$z(y) = H - \frac{1}{2}\left[\frac{1 - \left(\frac{\lambda\varphi}{2\pi B}\right)^2}{\sin(\theta - \alpha) + \frac{\lambda\varphi}{2\pi B}}\right]\cos\theta \qquad (4)$$

Height estimates are averaged over a surface resolution element of the radar image (picture element or pixel), typically tens of meters of diameter.

Repeat-pass InSAR. Now we consider a single-antenna SAR satellite that revisits the same area after several days or weeks. If there has been no significant change in the surface between the two acquisitions, we can perform essentially the same analysis as above and recover the same level of detail. In this case, we rewrite Eq. (3) as

$$\varphi = 4\pi\frac{dR}{\lambda}, \qquad (5)$$

or 2π times the round-trip distance difference in wavelengths. Rearranging Eq. $(2)_2$ and neglecting the small dR^2 gives:

$$dR \approx B\sin(\alpha - \theta) + \frac{B^2}{2R_1} \qquad (6)$$

For spaceborne geometries, we can make the parallel ray approximation [32] and ignore the last term on the right side of Eq. (6):

[b] This assumption is made in most literature derivations. It is not true for single-pass data acquisition.

[c] The actual generation of interferograms is much more sophisticated, cf. [20].

$$dR \approx B\sin(\alpha-\theta) = B_{\perp} \tag{7}$$

where $B_{\perp}$ is the projection of the baseline onto perpendicular to the line of sight.

Can we still recover topography if the surface has changed? It depends. If the relative positions of the radar scatterers within each pixel change more than one wavelength, we cannot perform the pixel-by-pixel comparison between the two images.

Now consider a case, where the surface displacement is coherent on a large-scale, i.e., across several pixels. In other words, the relative position of the radar scatterers does not change, but the ground moves up or down across several pixels. Now we can perform a phase comparison between the two images. The differential phase contains information about the radar beam range change, precise to a fraction of a radar wavelength, or about 1 cm for the C-band systems. To measure the surface displacement with this precision requires an accurate Digital Elevation Model (DEM) of the surface and very precise knowledge of the satellite positions.

Differential interferograms. If the second interferogram is acquired over the same area, sharing the orbit with the first pair so that both R_1 and θ are constant, we still can compare the phases of both interferograms. The second interferogram is acquired with a different baseline vector: (B',α'). Combining Eqs (5) and (7) we obtain

$$\varphi' = \frac{4\pi}{\lambda} B'_{\perp} \tag{8}$$

Therefore the ratio of the two phase-differences,

$$\frac{\varphi}{\varphi'} = \frac{B_{\perp}}{B'_{\perp}}, \tag{9}$$

is equal to the ratio of the parallel components of the baselines, and it is independent of topography.

Now consider two interferograms acquired over the same region as before, but at *two different times*, so that ground deformation caused by subsidence or uplift has displaced many of the pixels in the primed interferogram in a coherent manner. In addition to the dependence on topography, there is now an additional phase change caused by the ground displacement along the radar line-of-sight, ΔR:

$$\varphi' = \frac{4\pi}{\lambda}\left(B'_{\perp} + \Delta R\right) \tag{10}$$

The ground surface displacement ΔR adds to the topographic phase term and may cause interpretation problems. However, if the data in the first interferogram are scaled properly and subtracted from the second one, one obtains a solution that depends only on the displacement ΔR:

$$\varphi' - \frac{B_{\perp}}{B'_{\perp}}\varphi = \frac{4\pi}{\lambda}\Delta R \tag{11}$$

Since the quantity on the left is determined only by the phase differences in the respective interferograms and the orbit geometry, the line-of-sight displacement component ΔR is measurable at each pixel. A somewhat similar calculation can be done from a single interferogram and a DEM. First the topographic phase contribution is estimated from the DEM and the interferogram geometry, then it is subtracted from the interferogram.

Table 1 – Characteristic reservoir properties of the south Belridge and Lost Hills Diatomite

Parameter	South Belridge (source Aera Energy)	Lost Hills (source Chevron)
Porosity, %	40-70	35-66
Current water saturation, %	~45	~50
Current oil saturation, %	~45 (initial 30-70)	~45
Current gas saturation, %	~10	~5
Residual oil saturation to water, %	20	25
Liquid permeability, md	0.1-10	0.1-10
Average formation depth, ft	800	1900
Average productive thickness, ft	1000	800
OOIP in waterflood area (STB oil/acre-ft)	~2000	~1700
Oil API gravity	10-35	18-34

Table 2 – Characteristic time of pressure diffusion in years for the undamaged diatomite cycles in South Belridge at different injector-producer spacing; the hydraulic diffusivity data are from [30]

Cycle	Diffusivity sq. ft/day	5/16-acre	5/8-acre	1-1/4 acre	2.5-acre
G	0.573	8	31	122	299
H	0.135	32	130	520	1268
I	0.045	97	390	1559	3805
J	0.425	10	41	165	403
K	0.919	5	19	76	186
L	0.426	10	41	165	402
M	0.26	17	67	270	659

Table 3 – Orbit parameters from ESA

Orbit	**ERS-1&-2**	**JERS-1**	**RadarSat-1**	**Envisat**
Altitude (Km)	785	568	793-821	785
Inclination (degrees)	98.516	97.662	98.594	98.516
Period (s)	6027.907	5799.72	6042	6027.907
Repeat Cycle (days)	35, (3, 176)	44	24	35
Orbit type	Sun synchronous			
Ground Track Velocity (Km/s)	6.628	6.883	6.576	6.628
Launch Date	17 July 1991 (1) 21 April 1995 (2)	11 February 1992	4 November 1995	2 October 2001 (planned)
Decommisioned	10 March 2000 (1) partially active (2)	21 October 1998	Still active	
Interferometric Orbit Control	Good	Poor	Poor	Good

Table 4 – SAR parameters

	ERS-1&-2	**JERS-1**	**Radarsat-1 (fine, standard, wide)**
Frequency	C-Band (5.3 GHz)	L-Band (1.275 GHz)	C-Band (5.3 GHz)
Wavelength (cm)	5.66	23.5	5.66
Pulse Repetition Frequency (Hz)	1640-1720	1507-1606	1270-1390
Bandwidth (MHz)	15.5	15	30, 17.3, 11.6
Typical SNR (dB)	15	6	10 (standard)
Polarization	VV	HH	HH
Incidence Angles, Mid (Degrees)	19-27, 23	36-42, 39	20-49, 35
Nominal Swath Width (km)	100	75	50, 100, 150
Maximum Resolution—Range x Azimuth (m)	20 x 5	18 x 6	9x8, 25x8, 35x8
Typical Resolution (Num. looks)	20 (4)	20 (3)	9x9 (1), 25x28 (4), 35x30 (4)

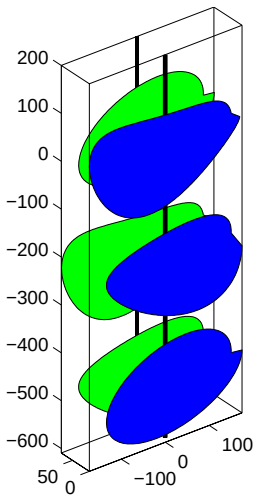

Fig. 1 – A 5/8-acre direct line pattern in South Belridge with vertically "fractured" wells. The cartoon is to scale and the dimensions are in feet.

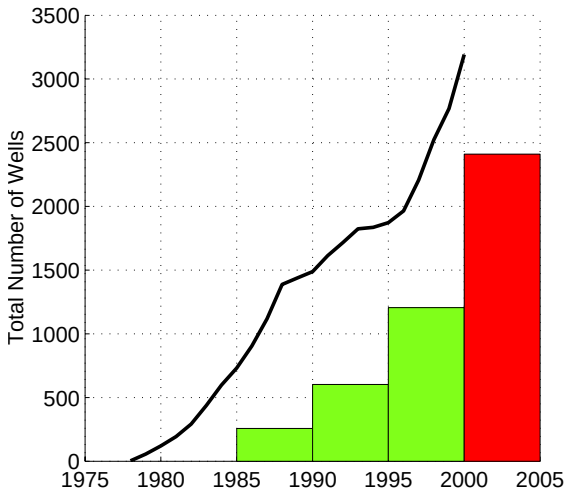

Fig. 2 – South Belridge Diatomite: the total number of active wells (line) and the cumulative number of failed wells lumped over five-year periods (bars); source: ftp://ftp.consrv.ca.gov/pub/oil/annual_reports/, and Aera Energy. The last bar on the right is our prediction that follows the exponentially growing trend: if the past rate of well failure continues, 20 well failures per month on average are predicted for 2000-2005.

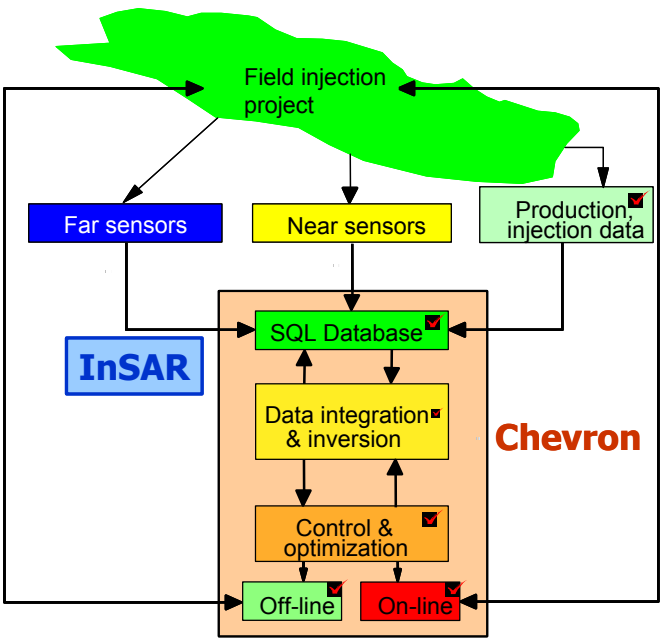

Fig. 3 - The proposed field wide system of surveillance and control. This paper will focus on the InSAR imaging of the field surface and the use of production/injection data. The controller system has been described elsewhere[2,6,19] and is being implemented by Chevron at Lost Hills.

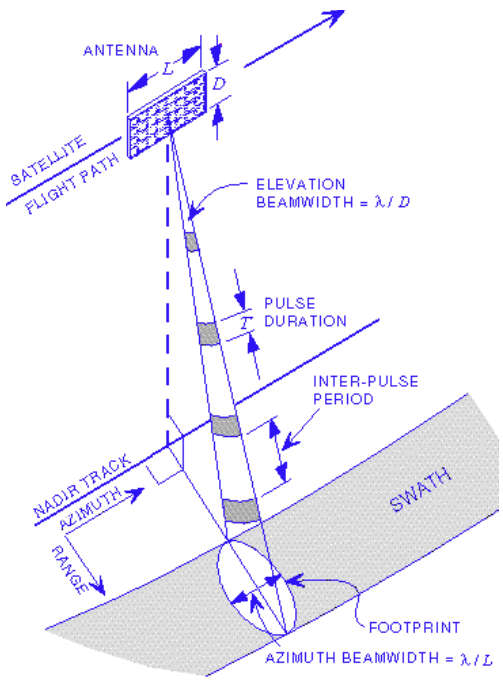

Fig. 4 – Geometry of SAR images from ESA.

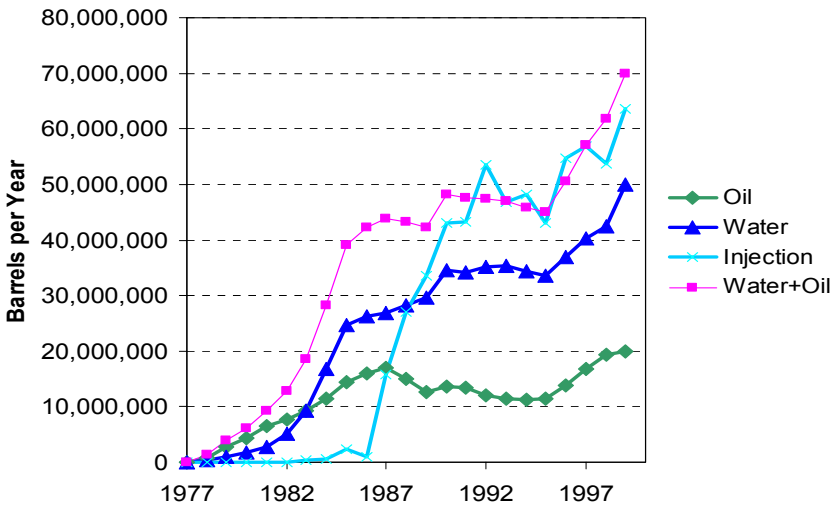

Fig. 5- Annual production and injection in the South Belridge diatomite. Globally, Belridge has always been on net withdrawal, although liquid production and injection rates were almost balanced in the last decade. Data source: CCCOGP, 1999 data are from Aera Energy.

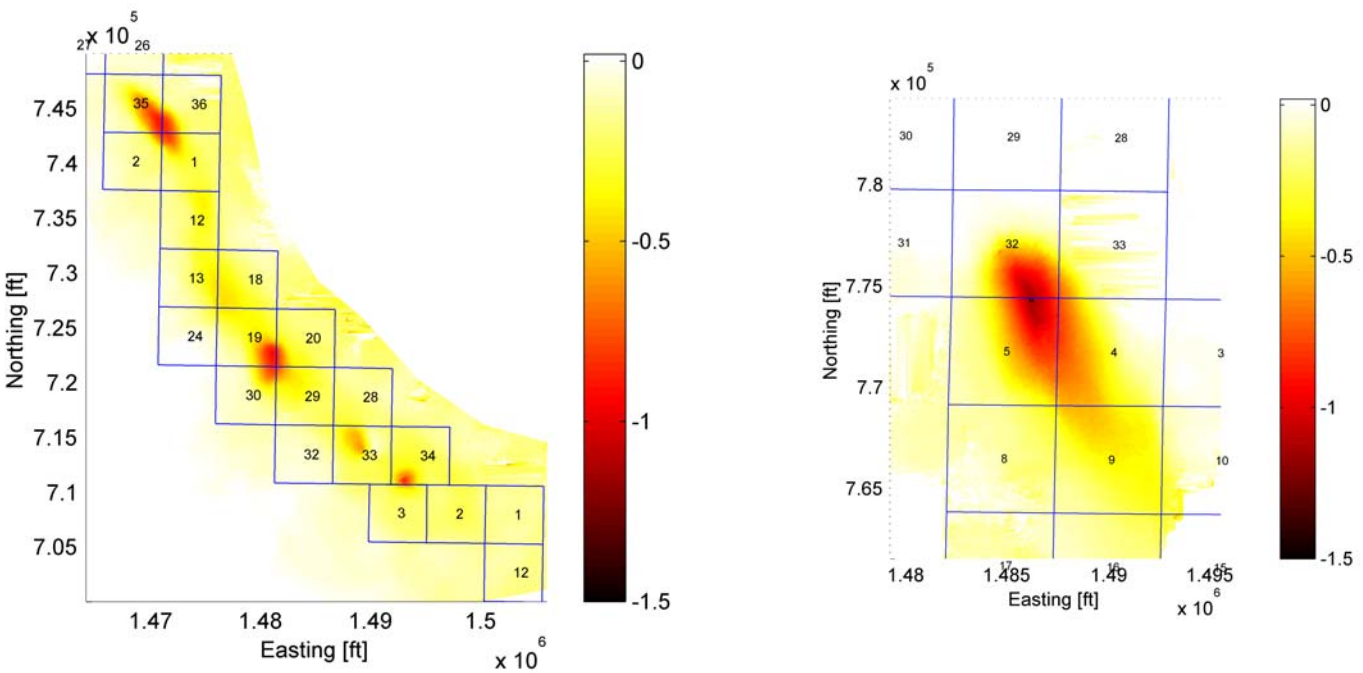

Fig. 6 – 1995/04-1995/05 subsidence rate maps in South Belridge (left) and Lost Hills (right), in mm/day. The 1995 interferogram is from the ascending orbit track, so the look direction from the ground to the radar is about ten degrees south of due west and roughly the opposite direction from the descending tracks. The angle from the vertical (23 degrees) is approximately the same for ascending and descending orbits. The data were processed on a 20-m grid.

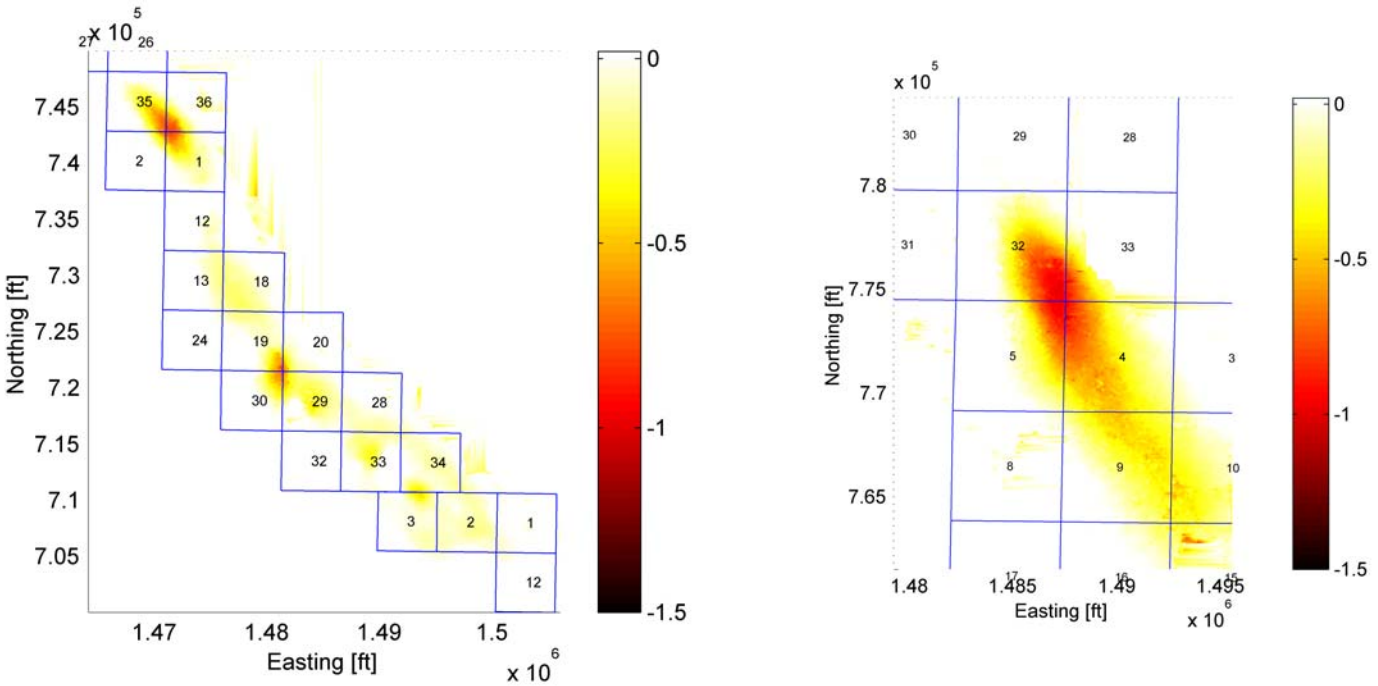

Fig. 7 1996/02-1996/04 subsidence maps in South Belridge (left) and Lost Hills (right), in mm/day. This interferogram was from a descending orbit, so the line-of-sight from the ground to the radar is about ten degrees south of due east.

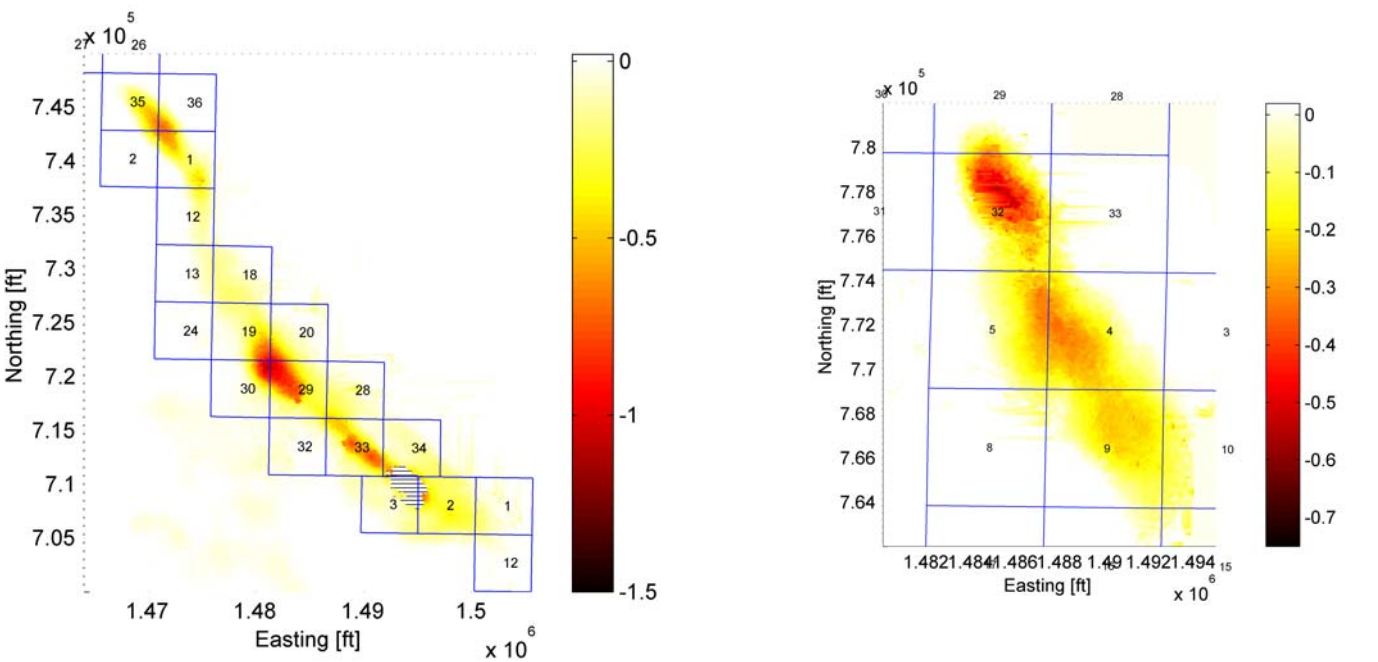

Fig. 8 1998/08-1998/11 subsidence maps in South Belridge (left) and Lost Hills (right), in mm/day. The lined spot in the SE part of S.B. (Sections 34, 3 and 2) is caused by too much subsidence in the 3 months separating the two images that made this descending interferogram. Note the different color scale in Lost Hills plot reflecting slower subsidence rate.

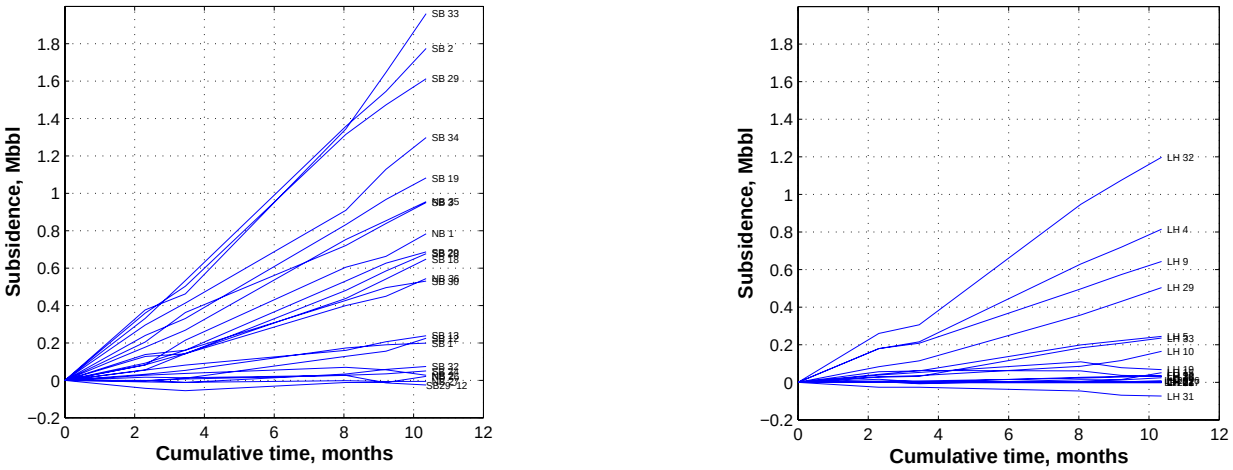

Fig. 9 – Annual subsidence in South Belridge (left) and Lost Hills (right) in 1999. Each curve depicts cumulative subsidence per section in millions of barrels.

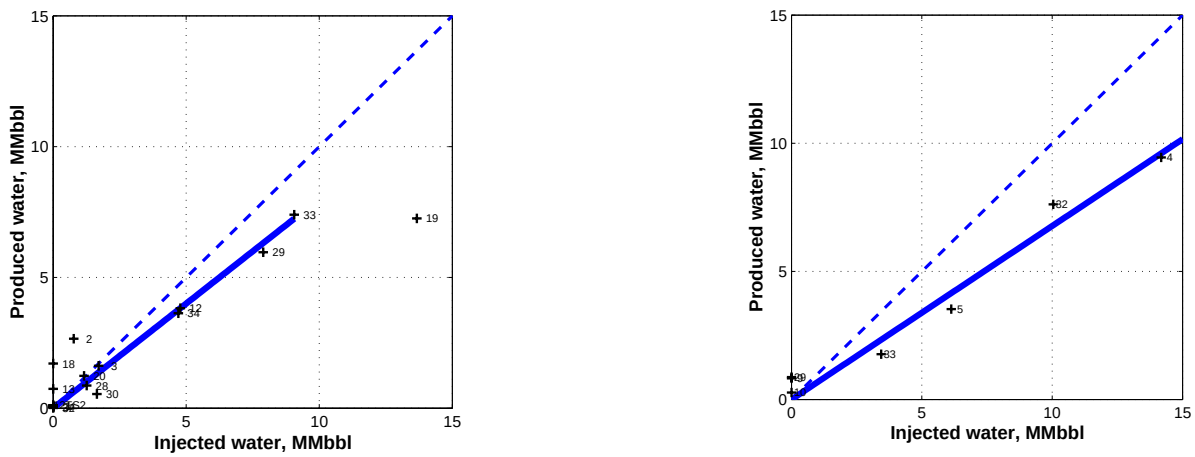

Fig. 10 – Produced vs. injected water by section of South Belridge (left) and Lost Hills (right). The correlation lines mean that 0.8 and 0.68, respectively, of the injected water was produced in most sections in 1999.

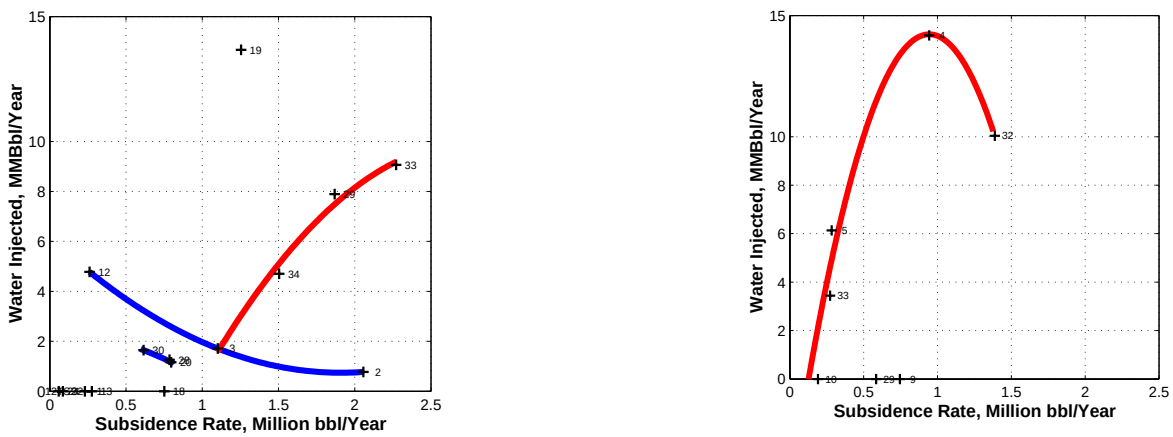

Fig. 11 – Trends of water injection vs. subsidence by section in the South Belridge diatomite (left) and in Lost Hills (right) in 1999. The expected trend of less subsidence with more water injection is not observed in sections with higher water injection, indicating rock damage by the respective waterfloods.

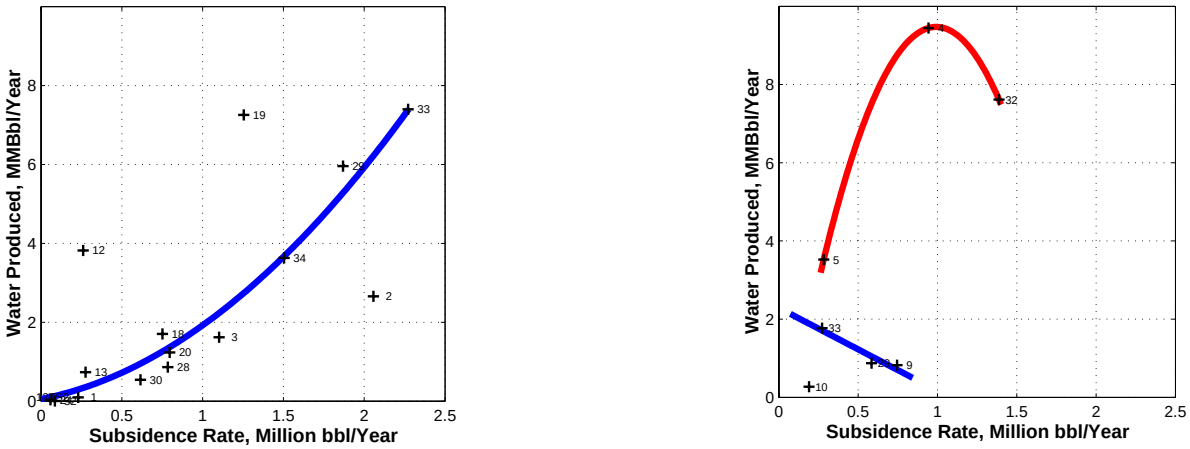

Fig. 12 – Trends of water production vs. subsidence in the South Belridge diatomite (left) and Lost Hills (right) in 1999. In general, more water produced corresponds to more subsidence, indicating rock damage by waterflood. In Lost Hills still there are sections, mostly on primary recovery, that follow an opposite trend.

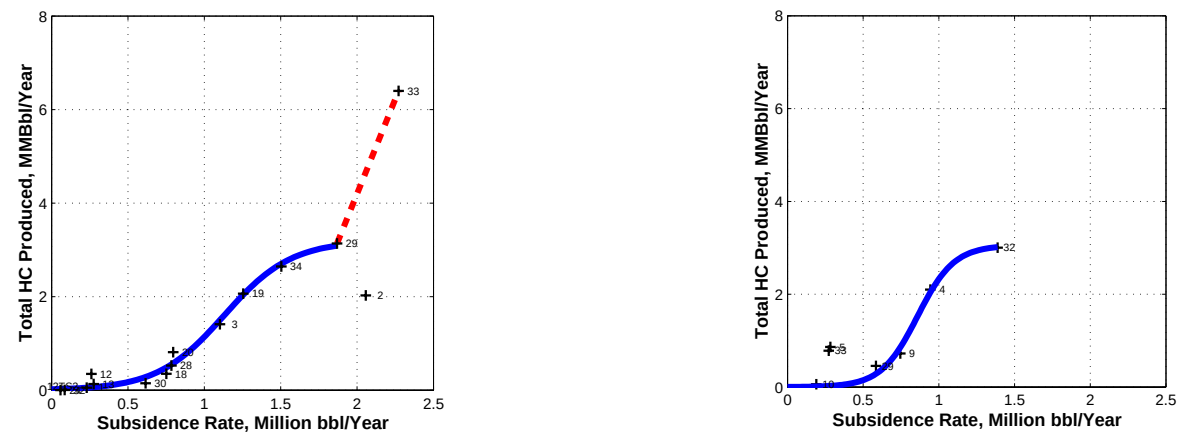

Fig. 13 – Trends in total hydrocarbon production vs. subsidence in the South Belridge diatomite (left) and Lost Hills (right) in 1999. In general, more subsidence corresponds to more hydrocarbons produced, indicating that compaction is an important production mechanism. These plots are somewhat deceiving because they mask different well densities in different sections.

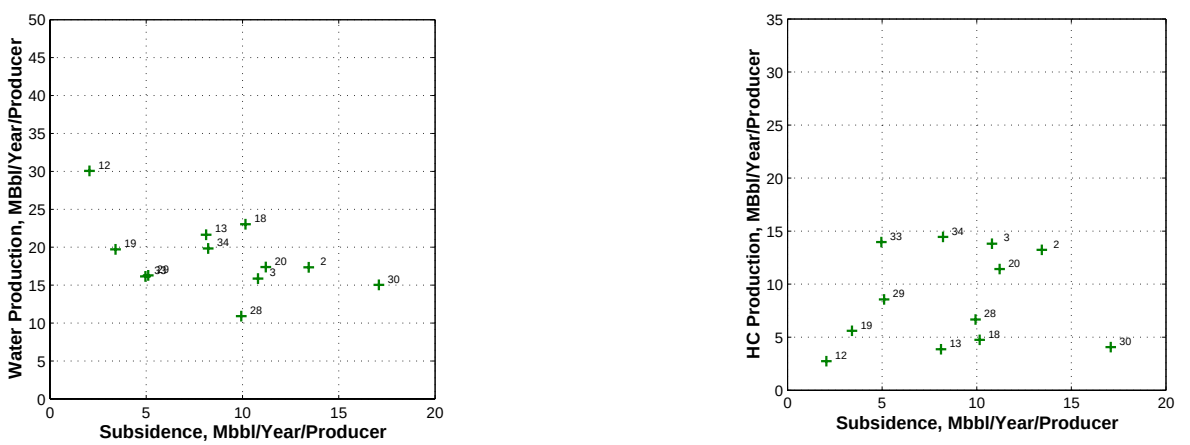

Fig. 14 – Annual specific water (left) and oil (right) production (per average well) vs. specific subsidence in sections of the south Belridge diatomite in 1999. It follows that the average well in Sections 29 and 33 does not produce the highest amount of water, one in Section 12 does. It also follows that an average well in Sections 32, 34, 2, and 3 produces the highest amount of oil. These trends reflect reservoir quality, response to waterflood and extent of rock damage.

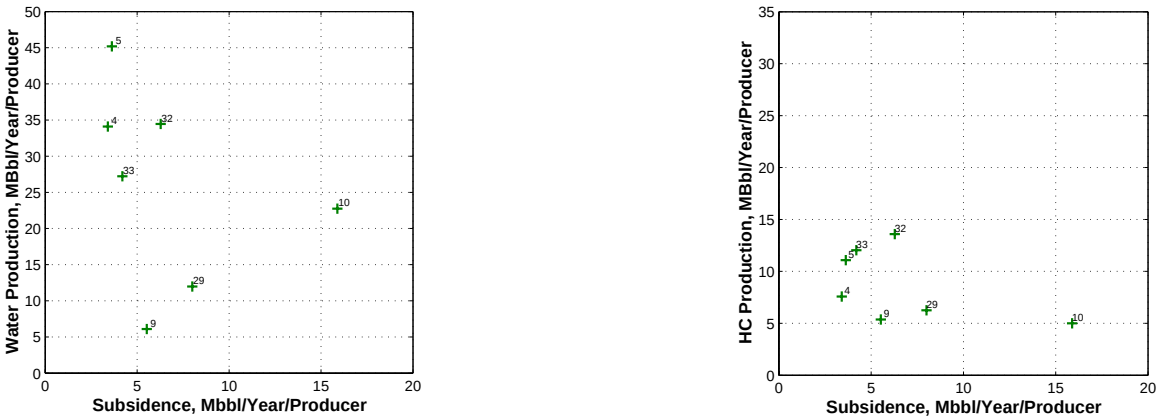

Fig. 15 – Annual specific water (left) and oil (right) production (per average well) vs. specific subsidence in sections of the Lost Hills diatomite in 1999. Note both water and oil production are comparable, but the specific subsidence is somewhat lower than that in the South Belridge. These trends reflect different reservoir qualities and depths.

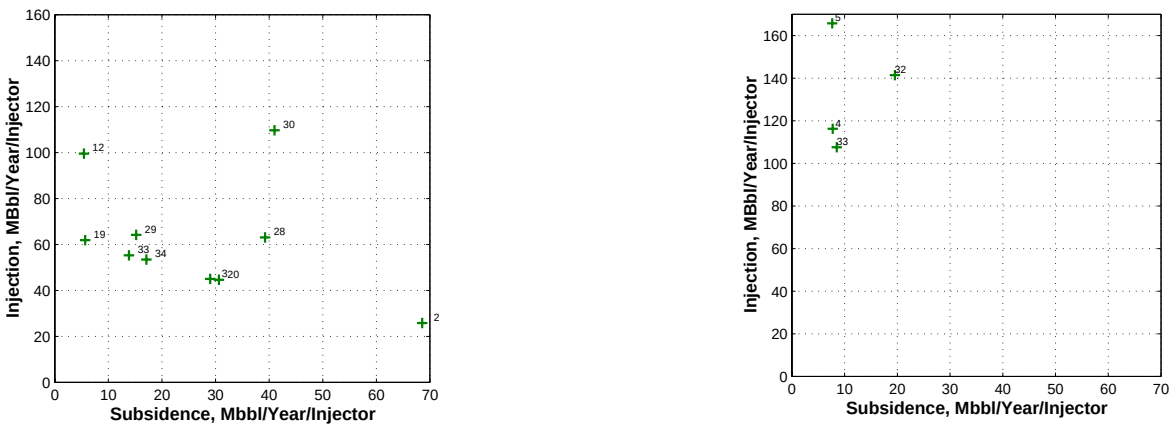

Fig. 16 – Specific annual water injection by section vs. specific annual subsidence (per injector) in Belridge (left) and Lost Hills (right) in 1999. Note that in Belridge, Sections 19, 29, 33, 34, 3, and 2 follow the same trend of less specific subsidence with more injection per well. In Lost Hills, the trend is inverted with more specific subsidence with more injection per well. This could mean that the Lost Hills diatomite is more damaged by the higher injection than that in Belridge, or that Sections 5 and 32 are over-injected.

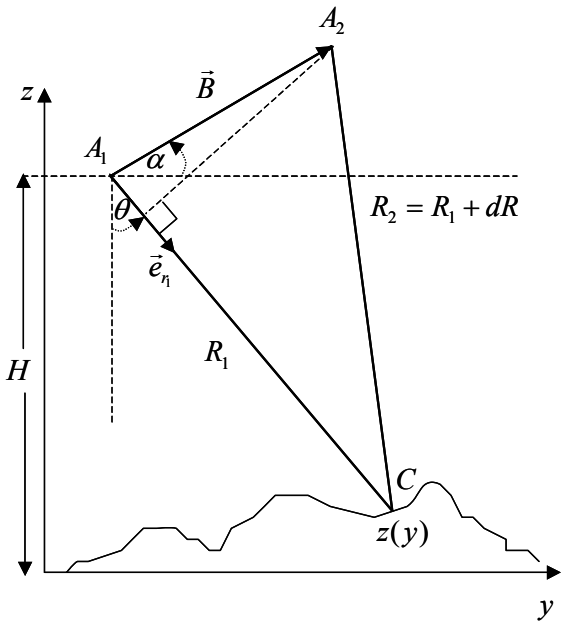

Fig. 17 – Imaging geometry for SAR interferometry. A_1 and A_2 are two radar antennas viewing the same surface simultaneously (spatial separation), or a single antenna viewing the same surface on two separate passes (temporal separation). $\vec{B}$ is the baseline vector, R_1 is the range of the first antenna, θ is the look angle of the radar with respect to vertical, α is the angle of $\vec{B}$ with respect to horizontal, and $\vec{e}_r$ is the unit vector along the line-of-sight R.

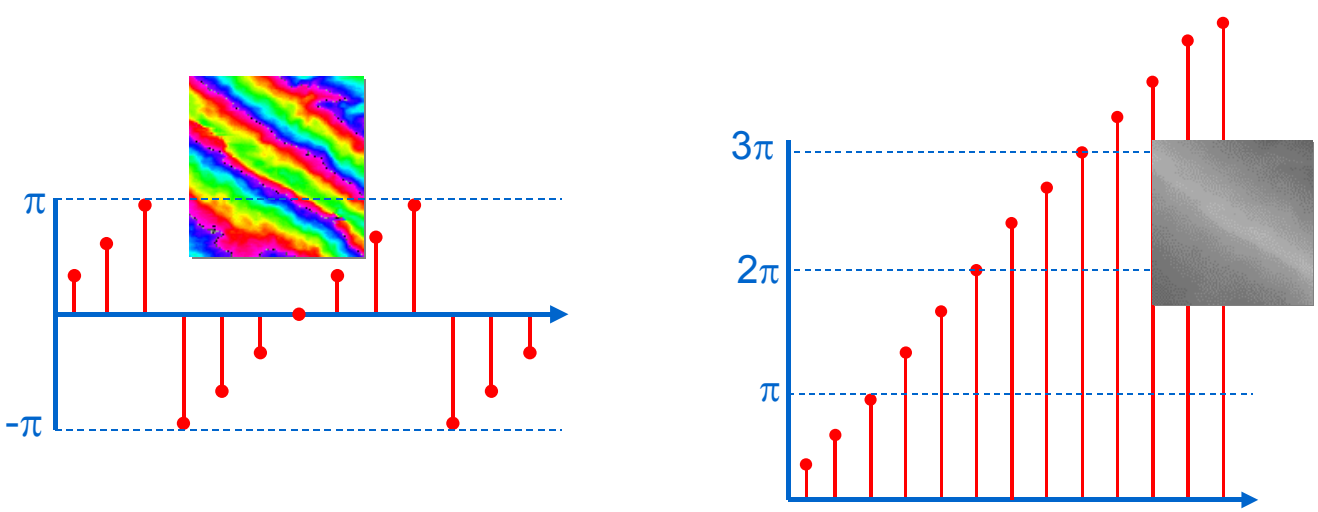

Fig. 18 – SAR interferogram phase unwrapping.